AIAA Aviation
16-20 June 2014, Atlanta, GA
45th AIAA Plasmadynamics and Lasers Conference

Characterization of a Spark Ignition System for Flameholding Cavities

Stefan Brieschenk*, Quentin Pontalier†, Alexandre Duffaut‡, Zachary J. Denman§, Anand Veeraragavan¶, Vincent Wheatley‖ and Michael K. Smart**

Centre for Hypersonics
The University of Queensland
Brisbane, Qld 4072, Australia

This paper presents an experimental investigation of a capacitive-discharge spark ignition system designed to promote ignition in CH_4- and C_2H_4-fuelled supersonic combustors. The purpose of this study is the characterization of the ignition system and the plasma generated in the discharge. Schlieren and luminescence imaging are used to visualize the temporal evolution of the spark plasma. Transient voltages and currents across the primary-side of the ignition coil and input-side of the ignition unit are recorded using a high-speed data acquisition system. Three different ignition coils are tested with two different spark plug gaps in an attempt to increase the performance of the ignition system which is evaluated through spatially and temporally integrated luminescence recordings as well as temporally integrated photo diode signals. The data suggests that an increase in performance of a factor of 4–5 over the baseline setup can be achieved. A capacitive ignition lead is used to assess whether or not any capacitance on the coil secondary side can increase the performance of the ignition system. The experiments have also shown that the ignition system parameters can be set to cause sufficient heating of the electrodes to support ignition from a combined glow-spark plug setup.

I. Introduction

Supersonic combustion ramjets typically rely on autoignition to promote combustion of the supersonic stream.[1] Ignition delay times in supersonic combustors are typically of the order of milliseconds for H_2 fuel, but orders of magnitudes longer for hydrocarbon fuels.[2] While hydrocarbon fuels have lower gravimetric energy densities compared to pure hydrogen fuel, hydrocarbon fuels are attractive for scramjet-powered vehicles due to their high volumetric energy densities and relatively simple storage requirements compared to cryogenic storage of liquid hydrogen. In a scramjet-powered vehicle, the liquid hydrocarbon fuel can be used as a heat sink for cooling critical components of the vehicle. The heat absorbed in the jet fuel can crack the liquid hydrocarbon fuel into gaseous compounds that are similar to H_2, CH_4 or C_2H_4, which typically have lower ignition delay times, higher combustion rates and faster mixing characteristics.[2,3]

*Post-Doctoral Research Fellow
†Occupational Trainee, Postgraduate Student at Paul Sabatier University, France
‡Occupational Trainee, Graduate Student at National Graduate School of Engineering ENSICAEN, France
§PhD Candidate
¶Lecturer
‖Senior Lecturer
**Professor

A CH_4- or C_2H_4-fuelled combustor can potentially achieve nearly as high thrust levels as compared to a H_2-fuelled combustor. This becomes apparent when comparing these fuels normalized to equal amounts of oxygen/air consumed as shown through reactions R 1–R 3. Assuming gaseous reaction products, the enthalpy of combustion is 242 kJ/mol (120 kJ/g) for H_2, 803 kJ/mol (50 kJ/g) for CH_4 and 1324 kJ/mol (47 kJ/g) for C_2H_4.

$$12\,H_2 + 6\,O_2 + 24\,N_2 \longrightarrow 12\,H_2O + 24\,N_2 - 2902\,\text{kJ} \quad \text{(R 1)}$$

$$3\,CH_4 + 6\,O_2 + 24\,N_2 \longrightarrow 3\,CO_2 + 6\,H_2O + 24\,N_2 - 2408\,\text{kJ} \quad \text{(R 2)}$$

$$2\,C_2H_4 + 6\,O_2 + 24\,N_2 \longrightarrow 4\,CO_2 + 4\,H_2O + 24\,N_2 - 2647\,\text{kJ} \quad \text{(R 3)}$$

From a heat-release point of view, CH_4 fuel reduces the achievable thrust by 17% whereas C_2H_4 fuel reduces the thrust by 9% compared to H_2 fuel. The heat release curves of stoichiometric H_2-air, CH_4-air and C_2H_4-air mixtures as functions of temperature are shown in Figure 1. These computations have been performed using NASA CEA.[4] For temperatures above 2000 K, the heat release decreases significantly due to dissociation of the combustion products CO_2 and H_2O. The dissociation temperature for CO_2 is slightly higher than that of H_2O, and for that reason, the heat release curves for CH_4- and C_2H_4-air mixtures intersect the heat release curve for H_2-air.

The most difficult aspects of CH_4 and C_2H_4 combustion in a supersonic combustor are the increased ignition and reaction delay times compared to hydrogen fuel. Methods for reducing ignition delay times are required if similar combustor geometries are to be used when fueling with CH_4 or C_2H_4 instead of H_2. Plasma generated by flowfield-external ignition sources can significantly reduce, virtually eliminate ignition delay times.[5–7] A number of literature reviews have been devoted to plasma-assisted ignition and combustion in supersonic flows.[8–10] Methods for ignition augmentation,[7] using flow-external energy sources[10] that directly or indirectly generate plasma,[9] include electric discharges in the combustible medium,[11] electric discharges in a plasma buffer gas (plasma torches),[12] microwaves[13] and lasers.[5–7] The purpose of this paper is the characterization of an off-the-shelf automotive capacitive-discharge spark ignition system to provide ignition in a cavity of a supersonic stream.

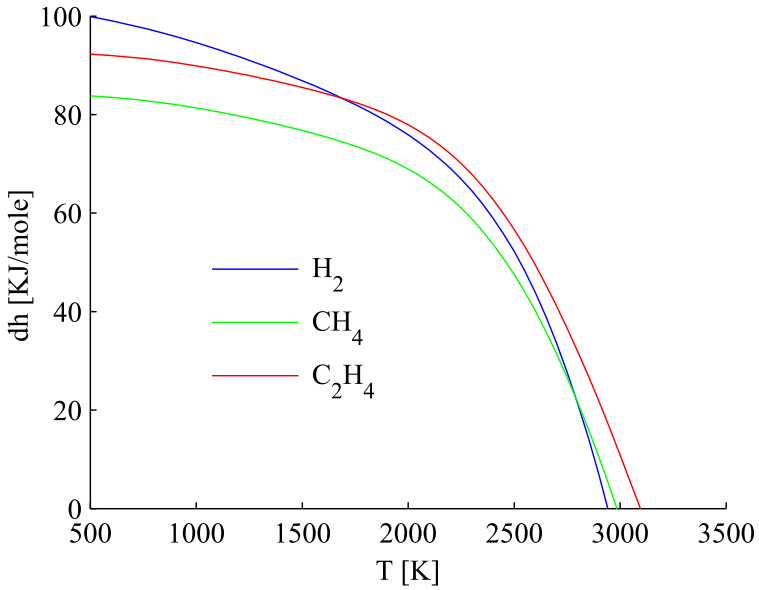

Figure 1. Heat release as a function of temperature for stoichiometric H_2-air, CH_4-air and C_2H_4-air mixtures.

flow properties		
stagnation enthalpy	h_0 [MJ/kg]	3.3
stagnation pressure	p_0 [MPa]	12.6
freestream velocity	u_∞[m/s]	2448
freestream temperature	T_∞[K]	340
freestream pressure	p_∞[kPa]	2.6
freestreem Mach number	M_∞[Pa]	6.6
freestream density	ρ_∞[g/m^3]	27
capture area	A_{in}[m^2]	$8.5e^{-3}$
captured mass flow rate	$\dot{m}_\infty$ [g/s]	560
supersonic combustor		
combustor entrance Mach number	Ma_c	3.5
combustor entrance temperature	T_c [K]	930
combustor entrance speed of sound	a_c [m/s]	580
combustor entrance velocity	u_c [m/s]	2005
combustor length	l_c [mm]	205
combustor transit time	t_c [ms]	0.10
flow power of captured stream	P_∞ [kW]	1850
max. combustor power H_2	$P_c^{H_2}$ [kW]	1960
max. combustor power CH_4	$P_c^{CH_4}$ [kW]	1625 (17% less)
max. combustor power C_2H_4	$P_c^{C_2H_4}$ [kW]	1780 (9% less)

Table 1. Overview of scramjet engine test parameters. Flow condition parameters are over a 1 ms test time. Freestream parameters refer to the thermal equilibrium flow conditions. Engine data taken for an angle of attack of zero degrees.

II. Scramjet Engine

A shape-transitioning scramjet engine[14,15] is used for this project. The baseline scramjet model was originally designed for H_2 fuel, and therefore features a relatively short combustor. An overview of the engine geometry is give elsewhere.[16] This study is part of an investigation that aims to determine the performance when this scramjet engine is fuelled with either CH_4 or C_2H_4 in combination with a spark ignition system to reduce hydrocarbon ignition delay times. This scramjet engine is scaled by 75% for testing in the T4 shock tunnel with respect to the original flight model. Ground testing will be performed in the T4 shock tunnel at the University of Queensland's Centre for Hypersonics.[17,18] An overview of the scramjet engine test parameters is given in Tab. 1. The table also shows the properties at the entrance of the combustor and gives an overview of the theoretical combustor powers using either H_2, CH_4 or C_2H_4 fuel. The Mach 7 scramjet engine has a maximum theoretical combustor power of 1960 kW when fuelled with H_2, which is approximately similar to the flow power of the captured air stream.

III. Repetitively Pulsed Ignition for Supersonic Flows

Promoting ignition in a supersonic stream using a plasma generator is only viable if the power requirement is lower than the performance gained from an increase in combustion efficiency, or reduction of drag by allowing for shorter combustor designs. One fundamental methodology to reduce the energy consumption of an ignition system for a supersonic combustor is to use a pulsed ignition source rather than a continuous ignition source. An approximate indicator of the required ignition repetition frequency using a repetitively generated plasma can be expressed as a simple function of flow and flame speeds as well as combustor length. The necessary periodicity of ignition in a supersonic stream is a function of flow and flame speeds as well as the combustor length. For an ignited gas region where the combustion is deflagrative, both, the combustion wave head and the tail of the flame travel downstream. The velocity of the combustion wave head u_h and combustion wave tail u_t are given by

$$\begin{aligned} u_h &= u_{st} + u_{fl} \\ u_t &= u_{st} - u_{fl} \end{aligned} \tag{1}$$

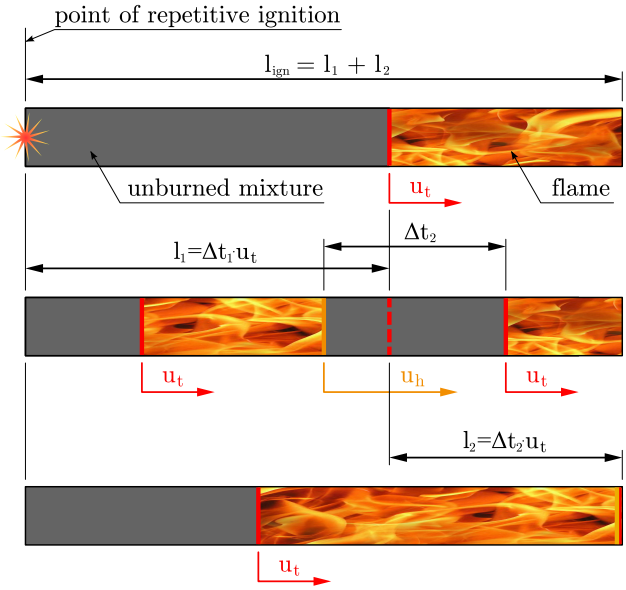

Figure 2. Repetitive ignition of a premixed supersonic stream undergoing deflagrative combustion. Direction of flow is from left to right.

where u_{fl} is the flame speed and u_{st} the velocity of the stream. The difference between these two velocities, u_{fl} and u_{st}, defines the required frequency f_{ign} to achieve complete ignition within the length l_{ign} in a one-dimensional flow path as depicted in Fig. 2. l_1 and Δt_1 refer to the duct length and time difference, respectively, of the non-ignited region at re-ignition, l_2 and Δt_2 refer to the additional duct length and time difference, respectively, required for the merging of the flame fronts u_h and u_t. The combustion wave head of the flame generated through a periodic ignition source catches up with the combustion wave tail of the previously ignited region through

$$\Delta t_2 = \frac{l_1}{u_h - u_t} \tag{2}$$

where The frequency f_{ign} with which ignition needs to occur can then be written as

$$f_{ign} = \frac{1}{\Delta t_1} = \frac{u_{st} + \frac{1}{2u_{fl}}\left(u_{st} - u_{fl}\right)^2 - u_{fl}}{l_{ign}} \tag{3}$$

The simplified assumption of constant flow and flame speeds is made in this derivation. Friction in an adiabatic, non-combusting, supersonic flow through a constant area duct, as described by the Fanno-flow model,[19] increases the entropy and reduces the static pressure with downstream distance. This reduces the velocity and Mach number of the supersonic flow. The addition of heat through combustion further reduces the velocity and Mach number due to the Rayleigh-effect,[19] which can eventually choke the flow.[20] This may result in increasing flame speeds, and in the extreme case, may result in a transition from deflagration to detonation. The influence of these effects however, can be canceled by introducing a divergence, of the order of several degrees, into the combustor section.[21] The ignition length l_{ign} is the necessary length for complete ignition of the stream to occur. The actual combustor needs to be longer due to the finite heat release time τ_{rct}.[22] According to Equ. 3, the necessary ignition frequency f_{ign} is directly proportional to the combustor ignition length l_{ign}. The parameter $\frac{f_{ign} l_{ign}}{a_c}$ plotted for various combustor Mach numbers Ma_c is shown in Fig. 3. Ignition frequencies need to be higher for externally-ignited combustors operating in deflagrative mode as compared to combustors operating in detonation mode. For a H_2 fuelled vehicle with a combustor entrance temperature of $T_c = 500\,\mathrm{K}$, operating at a global equivalence ratio of $\phi = 1$, the speed of sound in the combustor calculates to $a_c = 525\,\mathrm{m/s}$ assuming perfect mixing. For a combustor Mach number of $Ma_c = 1.2$ an ignition frequency of about $f_{ign} = 40\,\mathrm{kHz}$ becomes necessary to achieve complete ignition over a length of $l_{ign} = 100\,\mathrm{mm}$ with a turbulent flame speed of $u_{fl} = 50\,\mathrm{m/s}$. This condition is indicated in Fig. 3 with 'A'. For comparison, a combustor operating in detonative mode, where the detonation wave speed is the Chapman-Jouguet speed, which for a stoichiometric H_2-air mixture is in the order of $2000\,\mathrm{m/s}$,[23]

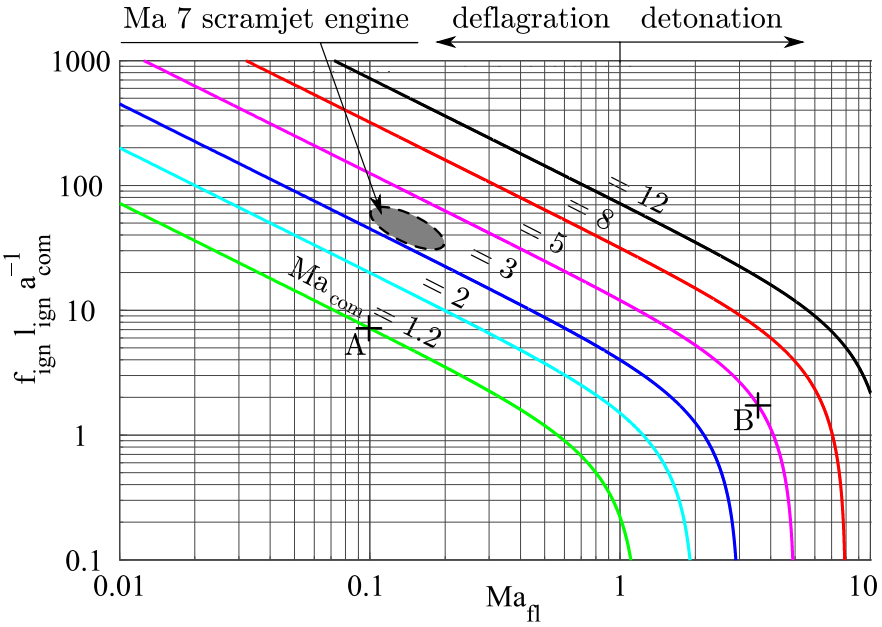

Figure 3. Required ignition frequencies for supersonic streams.

an ignition frequency of about 8 kHz is necessary for complete ignition over 100 mm at a combustor Mach number of $Ma_c = 5$. This condition is indicated in Fig. 3 with 'B'.

The combustor entrance flow properties of the scramjet engine investigated here have been outlined in Tab. 1. Using a turbulent flame propagation speed of Ma = 0.1–0.2 we get a frequency parameter of $\frac{f_{ign} l_{ign}}{a_c} = 30$–$70$. Using the data given in Tab. 1, we arrive at a required repetition frequency of 90-200 kHz. Such high ignition frequencies are technically hard to achieve, and for this reason, we combine the external ignition approach with a wall cavity that acts as a flameholder for limited amounts of time. A gas pocket ignited by an external ignition source can itself act as an ignition source for adjacent streamlines. This is the fundamental principle of providing ignition using a cavity-based, externally ignited flameholder. The purpose of the cavity is to reduce the required ignition frequency: a spark plug ignites the cavity flow, which then acts as an ignition source for the main flow in the combustor. Fig. 4 gives an overview of the fundamental processes for flameholding cavities. The autoignition conditions in the cavity are not met, and therefore, a flow external ignition source is required. In the simplest case, the combustion process in the cavity can be initiated by depositing thermal energy into the cavity using for instance a glow-plug. The deposited heat lifts the cavity flow above the autoignition threshold. The cavity flow can also be ignited directly, using for instance a spark discharge. The spark plasma can induce deflagrative and/or detonative combustion in the cavity. In an ideal situation, the combustor and the cavity would be designed such that the entrainment rate of both unburnt fuel and air into the cavity is sufficient to sustain the deflagrative combustion process in the cavity. In this case, the cavity would have to be ignited only once. If the entrainment rate of unburnt air and fuel into the cavity is too high or too low to sustain the deflagrative combustion process, the cavity flame extinguishes. A scramjet engine needs to operate over a wide range of Mach numbers, angles of attack and yaw. The large operating envelope of a scramjet engine makes it difficult for the flame in the cavity to sustain itself in all these possible scenarios. It is likely that sections of the operating envelope will lead to cavity flame-out, in which case a repetitive ignition source is required to re-ignite the cavity. Our analysis of the cavity flow for the scramjet engine discussed here[16] has shown that the cavity does not autoignite. A spark discharge can directly ignite the cavity flow. The actual energy deposited into the spark plasma in this case has to be above the minimum ignition energy (MIE). The unmixedness at the spark plug in the cavity flow, however, may be high enough to prevent the spark discharge from developing a deflagrative flame front. In this case, the spark discharge can still ignite the cavity as long as the deposited energy is sufficient to raise the temperature and pressure in the cavity above the autoignition threshold.

The MIE is the minimum theoretical amount of heat which could possibly lead to ignition. The concept of MIE draws the lower boundaries of ignition probabilities-a discharge with less energy does typically not

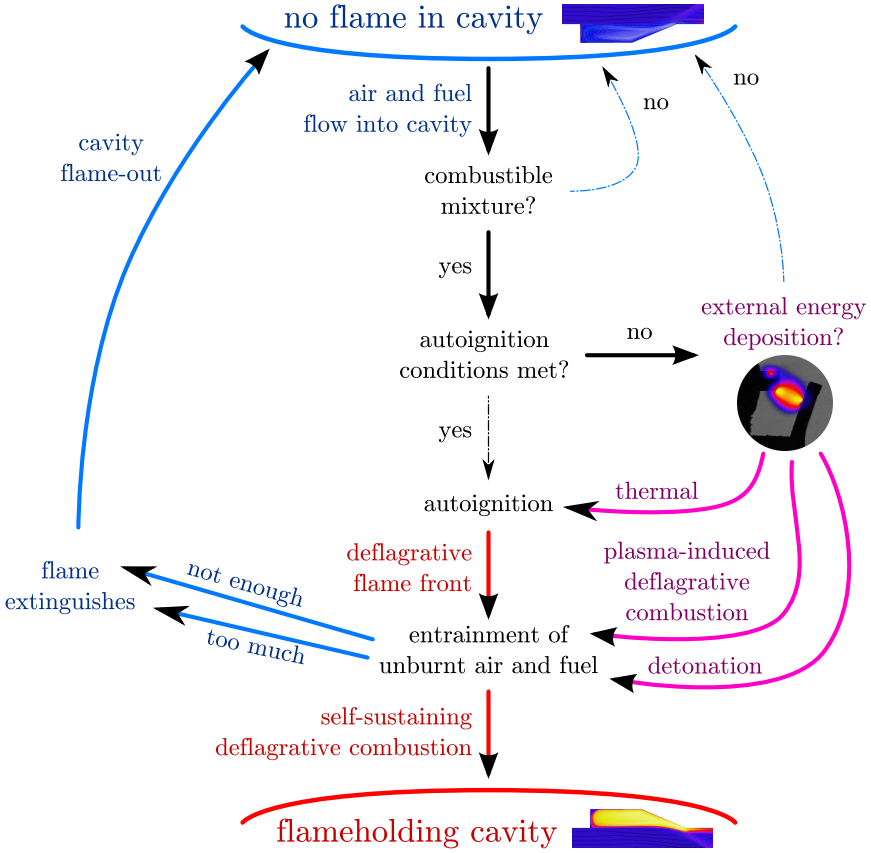

Figure 4. Fundamental processes for flameholding cavities.

lead to ignition; however, a discharge with a higher energy may or may not result in ignition. The minimum explosive concentration for pure CH_4 gas in air measures 4-5%. For a stoichiometric H_2-air mixture at a temperature of 300 K and a pressure of 1 atm, the MIE has been measured as 0.02 mJ.[24,25] For methaneair mixtures, the MIE is typically one order of magnitude higher.[24] Spark energies for practical applications where a high degree of flow turbulence is present are orders of magnitudes higher than the MIE. Spark energies range from 50–200 mJ in typical internal combustion engines. Previous spark-ignition experiments in supersonic streams using a laser source have been successfully performed with a laser-deposited energy of 300–400 mJ per spark.[5–7] Optical ignition using lasers allow the generation of plasma in the core of the stream, away from the wall. At this stage, however, there are no laser systems that can operate at the desired repetition frequencies, pulse energies and acceptable levels of wall-plug efficiencies. We have chosen a repetitively pulsed spark discharge system to provide ignition to the cavity flow, and the next chapters will outline the technical details and characterization of this system.

IV. Experimental Overview

An overview of the experimental setup is given in Fig. 5. A miniature spark plug (Rimfire Micro Viper Z3) is connected to an ignition coil powered by an automotive capacitive discharge ignition system (MSD-8 plus 7805). Three different ignition coils are tested, an overview of their specifications is given in Tab. 2. Coil A was used initially due to its small size and therefore easy implementation into the scramjet model and test environment. Two larger, more efficient ignition coils (coil B and C) are compared to evaluate potential performance gains. Two different ignition leads are used, a standard 8.5 mm spark plug lead with a resistance of 0.72 kΩ and a capacitive spark plug lead (Nology 012 001 041 HotWires) with a resistance of 0.75 kΩ and a capacitance of 67 pF. The ignition system is powered by a 1200 W DC power supply (Thurlby Thandar Instruments QPX1200). The coil primary voltage is measured directly using a differential probe (Testec TT-SI 9002 oscilloscope probe). The coil primary current is derived from measuring the voltage drop

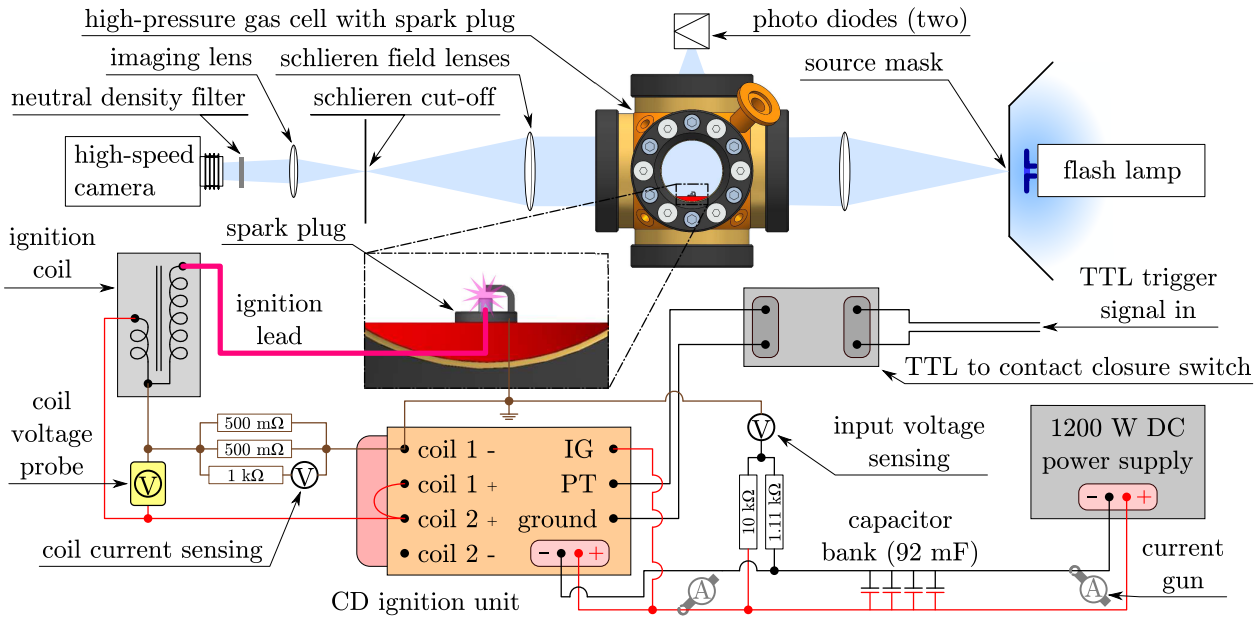

Figure 5. Schematic of experimental arrangement.

ignition coil	*A*	*B*	*C*
manufacturer	Accel	Speedmaster	MSD Ignition
part number	140032	PCE 382.1009 (Pc 91)	HVC-2 8261
R_{pri} [mΩ]	540	450	16
R_{sec} [kΩ]	5.88	3.80	0.03
L [mH]	1.54	6.60	0.25
turns ratio	61:1	100:1	70:1

Table 2. Overview of the three ignition coils tested.

over two 500 mΩ monitoring resistors (Arcol HS50) connected in parallel. A passive probe (Siglent 300 MHz passive oscilloscope probe, set to x1) is used to measure the voltage drop over these monitoring resistors. The transient input voltage of the ignition system is measured through a passive x10 divider using a 10 kΩ resistor, a 1.11 kΩ resistor and a passive probe (Siglent 300 MHz passive oscilloscope probe, set to x1). The input current of the ignition system before and after the capacitor bank is measured using two current guns (FW Bell CG-411A). To absorb the transient voltage requirements of the ignition unit, a 26 mF filter capacitor (MSD 8830) is connected to the input. This filter capacitor is typically sufficient when the ignition system is powered from batteries in an automotive application, however, the power supply used in this study required adding an additional 66 mF of capacitance (three 22 mF capacitors, RS 381-9037) to achieve stable operation of the ignition unit at an input voltage of 18 V and a spark frequency of 1300 Hz. A MOSFET is used to convert a TTL trigger signal into a contact closure to fire the ignition system. The ignition system setup discussed here is designed to provide high-frequency ignition in short duration shock tunnel experiments, where experimental windows are of the order of several milliseconds. For that reason, the bench experiments of the ignition system presented in this paper have typical durations of only 75 ms. With exception of the spark plug, no significant heating issues occur in the ignition components over that short time frame.

The spark plug is mounted in a gas cell which has multiple fused silica windows through which the spark event can be recorded visually. Schlieren visualizations are obtained using a dual-field-lens system. Achromatic field lenses with a focal length of 500 mm (Newport PAC096) are used in combination with an achromatic 260-mm-focal-length imaging lens. The spectral sensitivity of the optical elements ranges from 400-2500 nm. A Shimadzu HPV-1 monochrome high-speed CCD camera to record the spark discharge with a frequency of 1 MHz. The spectral sensitivity of the HPV-1 camera ranges from 400-950 nm. A circular source mask with an adjustable-diameter iris is used together with a photographic flash lamp (Bowens

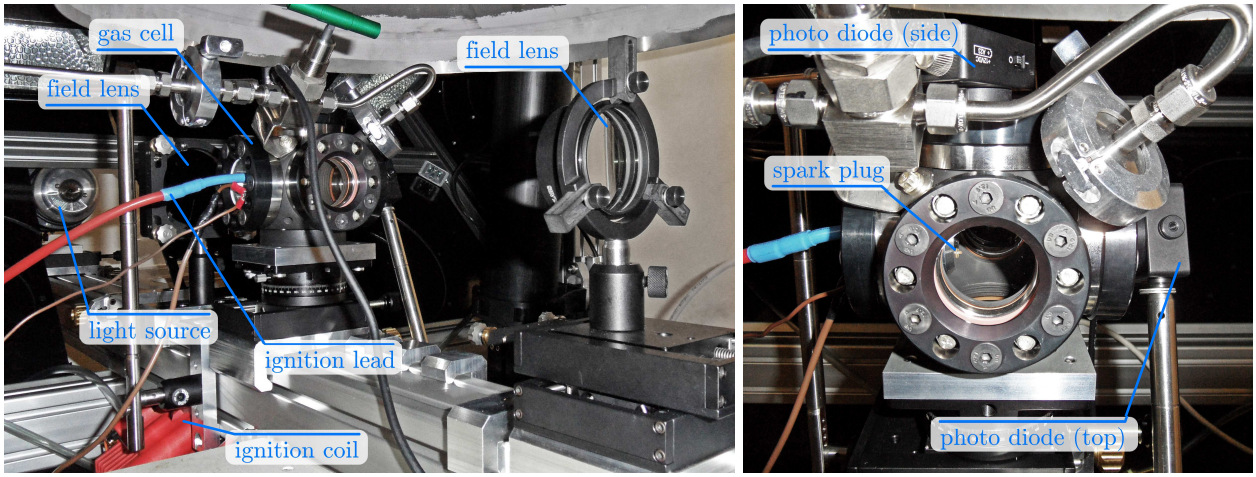

Figure 6. Photos of experimental arrangement.

Gemini Pro 1500) to provide illumination for the schlieren system. A circular schlieren cut-off is used to visualize density gradients equally in all directions. Luminosity recordings are obtained by removing the schlieren cut-off from the system and deactivating the flash lamp. The Shimadzu HPV-1 camera stores only 102 successive images and therefore, a Vision Research Phantom v611 monochrome CMOS high-speed camera was used for luminosity recordings that span over a 75 ms time window. The integration time per frame for the luminescence recordings using the Phantom v611 camera is set to the maximum (the period between the individual images) and a neutral density filter, with an optical density of one, is used to ensure that no saturation effects occur. The spectral sensitivity of the Phantom v611 camera ranges from 350 nm into the infrared to above 1050 nm. Two photo diodes (Thorlabs DET25K) are recording the luminescence of the spark in the 150–550 nm wavelength range. One photo diode is mounted on the test cell port that is located on the top of the spark plug, and a second photo diode is mounted to a test cell port that is located perpendicular to the principal axis of the spark plug. Fig. 6 shows photographs of the experimental arrangement with the photo diodes mounted. The luminescence recordings obtained with the cameras include the infrared signals that arise from the molten electrodes of the spark plug, whereas the signals recorded with the photo diodes do not.

A high-speed data acquisition system (National Instruments PCI-6123) with a time-resolution of 2 μs is used to record the voltage, current and photo-diode signals in the experiment. An experiment controller (LabSmith LC880) triggers the ignition unit, the data acquisition system and the schlieren/luminescence recording system. With exception of the schlieren visualizations, the gas cell is filled with air at atmospheric pressure, which is similar to the combustor pressure observed in the scramjet engine. The limited sensitivity of the small-scale schlieren system used here does not allow resolving the density gradients generated by the spark discharge in one atmosphere of pressure. For this reason, the schlieren visualizations were conducted with the test cell filled to 12 bars of pressure. Argon was used instead of air to visualize the transient behavior of the spark discharge plasma. Argon has a plasma lifetime that is significantly longer than that of air, allowing the high-speed visualization of the plasma with the equipment used for the tests presented in this paper.

Without any RPM module connected to the ignition unit, ignition frequencies of up to 1400 Hz could be achieved in the tests presented here. The maximum ignition frequency is a function of the supply voltage, as shown in Fig. 7. The ignition frequency linearly increases with the supply voltage up to 18 V. For higher input voltages, the maximum repetition frequency reduces. We have chosen to perform all experiments at an input voltage of 18 V and a frequency of 1300 Hz, slightly lower than the maximum frequency, to ensure that the ignition unit does not miss a spark in any of the configurations tested. In the experiment, a spark is generated every 769 μs for a total duration of 70–75 ms. Approximately 90 spark discharges occur at the spark plug during a single experiment. Longer running times are possible, but we will show later that this leads to melting of the spark plug electrode and ground strap.

Six different configurations have been characterized in this paper. An overview of these configurations is given in Tab. 3. The baseline setup, configuration *I*, uses coil A and a spark plug gap between the center

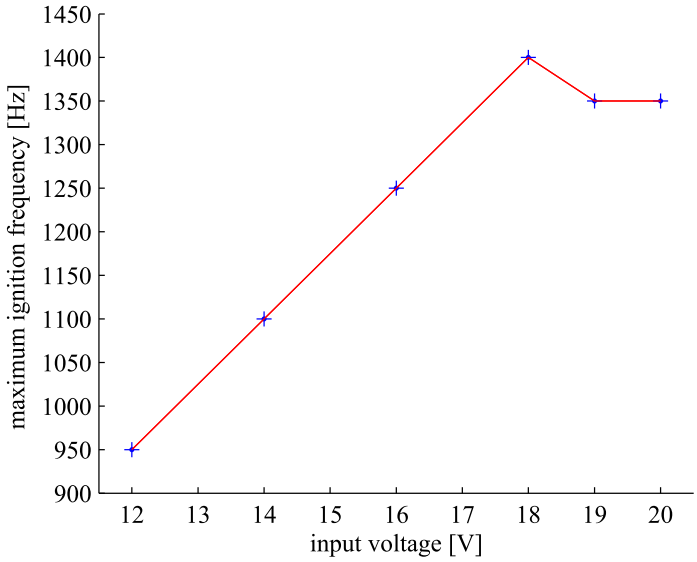

Figure 7. Maximum ignition frequency measurements of the ignition unit as a function of supply voltage.

configuration	*I*	*II*	*III*	*IV*	*V*	*VI*
ignition coil	A	B	B	C	C	B
spark gap [mm]	0.54	0.54	0.74	0.54	0.74	0.54
ignition lead	standard	standard	standard	standard	standard	capacitive
curves in Figures	solid green	solid blue	dashed blue	solid red	dashed red	solid magenta

Table 3. Overview of the six configurations tested.

electrode and the ground strap of 0.54 mm. Configuration *II* compares potential performance gains using a more efficient ignition coil. Primary and secondary resistances of coil B are comparable to that of coil A, however, coil B features a closed iron core, rather than an open iron core and has a larger inductance. The closed iron core leads to a larger footprint and increased weight, but reduces inductance losses with the net result of higher conversion efficiencies from the coil primary to the coil secondary side. Configuration *IV* compares potential performance gains using a closed-iron-core coil with significantly lower coil primary and secondary resistances as well as a significantly lower inductance. The low coil winding resistances of coil C allow for higher coil currents and the possibility of increased spark performance. Ampere's Law states that the magnetic field strength is proportional to the current, higher currents in the coil should lead to higher spark energies as long as the gain is balanced with the Joule heating losses, which scale with RI^2. The increased Joule heating in coil C has no effect for the short-duration experiments presented here. Configuration *III* and *V* are similar to configurations *II* and *IV*, respectively, but use larger spark gaps of 0.74 mm. Configuration *IV* is similar to configuration *II* but uses a capacitive ignition lead. Ten experiments are conducted for each of these configurations and the results given in this paper are the average results of 10 individual tests.

V. Results and Discussion

V.A. Transient Voltages and Currents

A comparison of the transient coil primary voltages and currents as well as average powers during a spark discharges for the coils tested is given in Fig. 8. Coil A and B show fife successive maxima in the transient voltage and current curves and have spark durations of 250 μs and 210 μs, respectively. Peak voltages, currents as well as the phase shift between the two are similar for both coils. The average power consumption of the ignition unit is 625 W and does not vary significantly between the different configurations tested. Coil B shows peak powers 36% higher and average spark powers 18% higher compared to Coil A. The spark energy of coil B is also increased by 18% from 261 mJ to 307 mJ. The electrical efficiency of the ignition unit is 21%

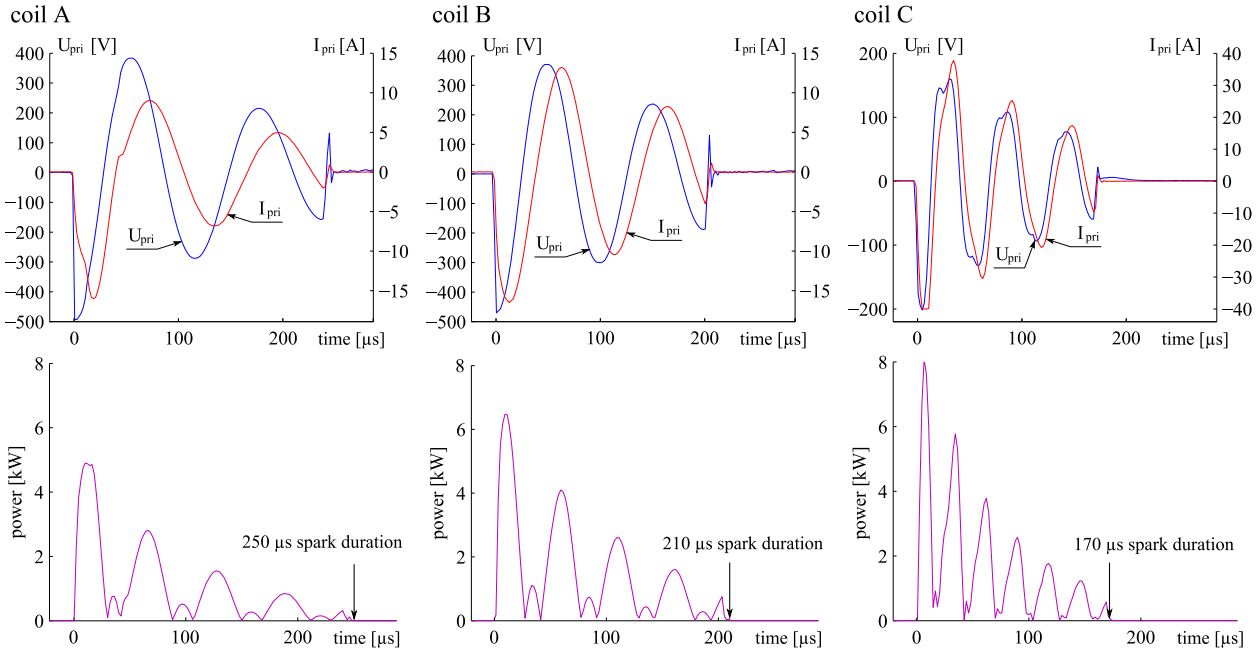

Figure 8. Transient coil primary voltage and current (top) as well as average power (bottom) during a spark discharge for the coils tested.

configuration		*I*	*II*	*III*	*IV*	*V*	*VI*
input power	P_{in} [W]	647 ± 8	633 ± 4	610 ± 4	628 ± 3	617 ± 3	609 ± 2
peak primary voltage	$\widehat{U}_{pri}$ [V]	> 500	> 500	> 500	210	210	> 500
peak primary current	$\widehat{I}_{pri}$ [A]	18	18	18	> 40	> 40	18
peak secondary voltage	$\widehat{U}_{sec}$ [kV]	33	50	50	15	15	50
peak spark power	$\widehat{P}$ [W]	4823 ± 33	6559 ± 34	6383 ± 46	8047 ± 45	8040 ± 64	6492 ± 9
average spark power	$\overline{P}$ [W]	339 ± 3	399 ± 3	394 ± 3	394 ± 2	384 ± 3	395 ± 2
electrical efficiency	$\frac{\overline{P}}{P_{in}}$ [-]	0.52	0.63	0.65	0.63	0.62	0.65
average spark energy	$\overline{E}$ [mJ]	261 ± 2	307 ± 2	303 ± 3	303 ± 1	295 ± 2	304 ± 1

Table 4. Results for the six different configurations tested. Data averaged over 90 spark discharges per experiment, and 10 experiments per configuration. These results represent the data from 5400 spark discharges.

higher for coil B. The results of this performance comparison are listed in Tab. 4. The coil secondary voltage and current are not measured in the experiment, they can only be estimated using the coil turns ratio. The higher turns ratio of coil B implies a higher coil secondary voltages as compared to coil A.

Coil C shows seven successive maxima in the transient voltage and current curves and has a spark duration of 170 μs. The low winding resistances of this ignition coil result in peak voltages that are 58% lower and peak currents that are 2.2 times higher. Coil C shows peak powers 67% higher and average spark powers 16% higher compared to Coil A. The spark energy is increased by 16% from 261 mJ to 303 mJ. Compared to coil B, the peak power is increased by 23%, while the average spark power and energy are slightly lower. The electrical efficiency of the ignition unit when operating with coil C is similar to that when operating with coil B. Whether or not the ignition performance, measured here in terms of the coil's ability to generate plasma, of coil C is higher than that of coil B cannot be determined from the measured electrical data. This question will be answered through the recorded luminescence data that will be presented in the following sections.

We could not observe a significant change of the coil primary voltage, current and average power for the two different spark plug gaps. The data given in Tab. 4 suggests no significant difference between configurations *II* and *III*, and *IV* and *V*, respectively. Using the capacitive spark plug lead instead of the standard spark plug lead did also not have a significant effect on these parameters. The results obtained for configuration *VI* are similar to those of configuration *II*.

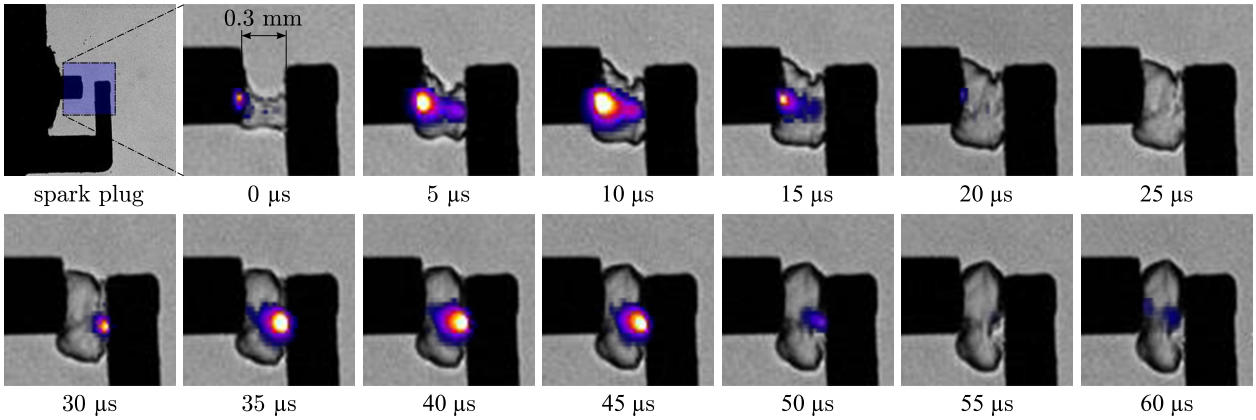

Figure 9. Time-resolved luminescence recordings superimposed on schlieren visualizations for a single spark event. Recording speed is 1 Mfps, integration time per image is 500 ns.

V.B. Time-resolved schlieren and luminescence recordings of the spark discharge

The plasma generated in the spark discharge oscillates in the same fashion than the voltage and current traces shown in Fig. 8. This was observed from time-resolved luminescence recordings, some of which are presented in Fig. 9. Here, a luminescence recording is superimposed on a schlieren recording, obtained at a recording speed of 1 Mfps and an integration time of 500 ns per image. The gas pressure was increased to 12 bar to counteract the limited sensitivity of the schlieren system. Argon was used instead of air due to its significantly longer plasma lifetime, allowing for the high-speed luminescence recordings. The configuration tested here is similar to configuration *IV* (coil C is used), however, the spark plug gap is set to 0.3 mm. The breakdown voltage U_P required to initiate a plasma at the spark plug can be calculated using Paschen's law, where p is the pressure of the gas and d is the spark gap.

$$U_P = \frac{Apd}{ln(pd) + B} \tag{4}$$

A and B are constants that are dependent on the gas species. For argon at 12 bar of pressure and a spark gap of 0.3 mm the breakdown voltage can be calculated to ≈ 7 kV. The first voltage maximum for coil C is 210 V, which translates into a secondary voltage of 15 kV using the specified turns ratio of the ignition coil (Tab. 2). At this point, the voltage and current on the secondary side of the ignition coil can only be estimated by using the specified turns ratio and the measured voltages and currents at the primary side of the ignition coil. Further experiments where the coil secondary voltage and current are measured need to be conducted in the future. The third voltage maximum is just above the breakdown voltage and it can be observed from the visualizations in Fig. 9 that only the first two of the seven power spikes (see coil C in Fig. 8) generate a significant amount of plasma at the electrodes in this test. The third power spike still generates some plasma, and the coil secondary voltage seems to be just above the breakdown voltage, whereas the remaining power spikes do not generate any measurable luminescence in our experimental setup. Using an assumed efficiency of 20% for coupling the electrical energy on the primary side of the ignition coil into the gas gives 60 mJ for heating the gas volume between the electrodes. The rest of the energy, here 243 mJ, would be dissipated as heat in the secondary side of the ignition coil. These energies are only rough estimates, more experiments have to be performed in the future where the voltage and current on the coil-secondary side are measured.

The schlieren visualizations can now be used to extract the volume of the hot gas pocket generated from the discharge to estimate its approximate mean temperature. The volume and temperature of the hot gas pocket are important for computational fluid dynamic simulations of the spark ignition process. For the visualization shown in Fig. 8, the hot gas pocket after the discharge has the shape of a cylinder with a diameter of 2.4 mm and a height of 0.3 mm, giving a volume of $V_p = 1.4\,mm^3$. The hot gas cloud does not expand further after 60 μs, and has equalized its pressure with the surrounding gas. Assuming a constant c_p for argon while neglecting the volume work that the expanding hot gas pocket has performed we can

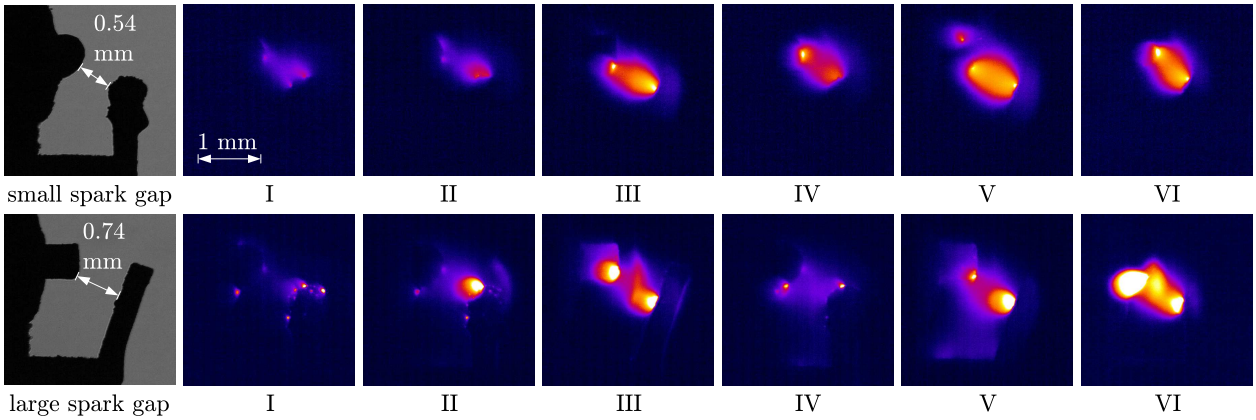

Figure 10. Time-integrated luminosity recordings for the different test configurations after the first spark event (top, average of 10 tests, i.e. 10 spark discharges per image) and after 90 spark events (bottom, average of 10 tests, i.e. 900 spark discharges per image). Small and large gap refer to an effective spark gap of 0.54 mm and 0.74 mm, respectively.

configuration	*I*	*II*	*III*	*IV*	*V*	*VI*
after first discharge						
relative to conf. *I*	1.0	1.5	3.5	3.7	5.0	3.0
relative to conf. *II*		1.0	2.3			2.6
relative to conf. *IV*				1.0	1.4	
after 90 discharges						
relative to conf. *I*	1.0	3.9	4.6	3.2	5.3	10.5
relative to conf. *II*		1.0	1.2			2.7
relative to conf. *IV*				1.0	1.7	

Table 5. Relative performance of ignition configurations from spatially integrated luminescence signals.

estimate the mean temperature using the following equation where $\Re$ is the gas constant.

$$\Delta T = \frac{\Delta E T_1 \Re}{c_p V_p p_1} \tag{5}$$

The average temperature of the 1.4 mm^3-hot-gas volume using the above equation is calculated to be 4600 K. The approach used here to visually measure the size and calculate the average temperature of the hot gas pocket after the spark discharge has not been applied to the experimental configurations *I*–*VI* where the spark is generated in air at ambient pressure due to signal-to-noise issues in the schlieren and luminescence recording system at these conditions.

V.C. Spark-averaged Luminescence recordings

A comparison of the spark discharge luminescence of configurations *I*–*VI*, integrated over the duration of a single and all 90 spark discharges is shown in Fig. 10. The spatially integrated signals, relative to the baseline configuration (configuration *I*), for the luminescence images shown in Fig. 10 are given in Tab. 5. The figure also shows an image of the small and large spark gaps used. The spark plug used for the small gap discharge tests (configurations *I*, *II*, *IV* and *VI*) was stressed in a previous test that lead to the partial melting of the electrode and the ground strap. This increased the effective spark gap from 0.3 mm to 0.54 mm. The experiments presented in this section had an overall duration of 75 ms each which did not lead to any significant damage of the electrodes during testing. A comparison of configuration *I*, *II* and *IV*, which compares all three coils using the 0.54 mm spark gap after the first spark discharge (top images of Fig. 10) shows that the discharge using coil B generates 150% more luminescence than coil A, and coil C generates 370% more luminescence than coil A. Increasing the spark plug gap by 37% leads to an additional increase in the luminescence signal, with signals of 230% for coil B and 140% for coil C compared to the baseline. The capacitive ignition lead generates a luminosity signal that is 260% compared to that of the baseline. Coil C in configuration *V* with the increased spark gap generates the strongest spark with an integrated luminosity

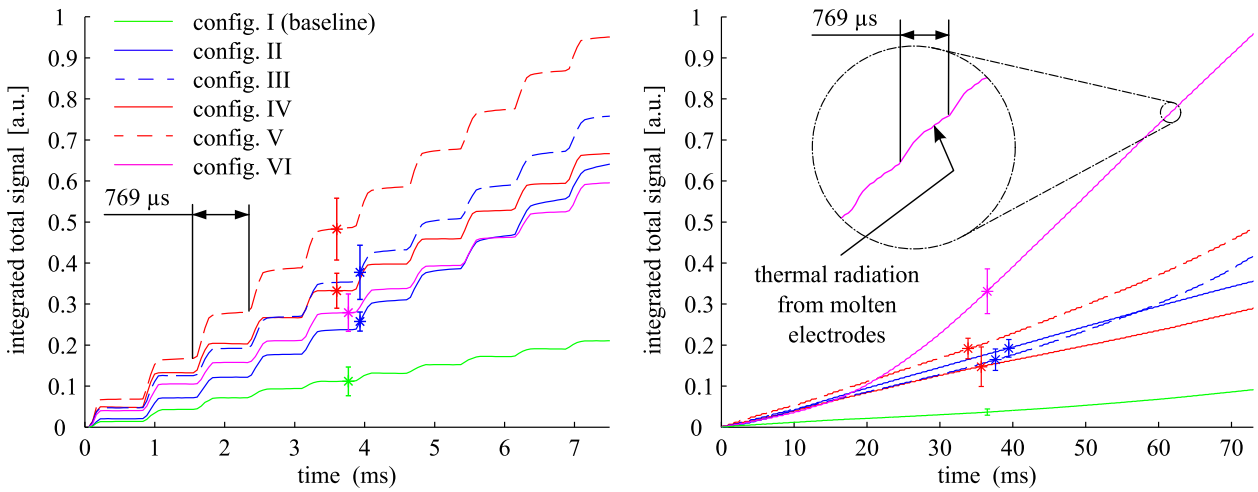

Figure 11. Integrated luminescence from time-resolved camera recordings.

signal that is 500% higher than that of the baseline configuration. This configuration also generates the most homogeneous plasma distribution and largest plasma volume. The general conclusions and trends derived from these data do not change when integrating over the entire 90 spark discharges rather than just the first spark discharge. While data integrated over 90 sparks should yield a more representative set of data, the discharges in the spark plug cause small sections of the electrodes to melt, which leads to an additional signal due to thermal radiation of the molten regions. This effect becomes clear when inspecting the integration data plotted over time, as shown in Fig. 11. The integrated luminescence data should have the shape of step functions that occur after every time period (769 μs) between individual discharges. Once the spark discharge has happened, the integrated luminescence signal should remain constant until the next spark discharge occurs. While this is given for the first couple of milliseconds, the progressive shape of the luminescence curves after 10 ms indicates that the additional signal due to thermal radiation from the molten electrodes is significant. Configuration VI causes the highest amount of electrode heating, and although the first spark (Fig. 10 and Tab. 5) in that configuration is 340% stronger than the first spark of the baseline configuration, it is difficult to tell whether or not this is also the case over the entire 75 ms of the experiment. This question will be answered by analyzing the recorded photo diode signals in the following sections.

V.D. Photo Diode Signals

The spectral sensitivity range of the photo diodes ranges from the ultraviolet into the visible green and therefore, the signal does not include the thermal radiation signal in the visible yellow, red and infrared part of the spectrum occurring at the molten spark plug electrodes. The time-integrated photo diode signals for the test configurations using the 0.54 mm spark gap (configurations I, II, IV and VI) are shown in Fig. 12. The degressive shape of the curves suggests that the effective energy used to generate the plasma reduces as the electrode gaps begin to heat up and melt. Both, coil B (configuration II) and C (configuration IV) outperform the baseline configuration in a similar fashion as was observed previously. Adding capacitance to the secondary side of the ignition coil (configuration VI, coil B) generates a spark that is as roughly as strong as the spark generated with coil C (configuration IV) for the first few milliseconds. For longer times, however, the additional capacitance causes a significant amount of electrode heating and the actual spark luminescence decreases below that of configuration II, which also uses coil B but without the capacitive ignition lead. Both photo diodes record similar trends, however, for the photo diode that is mounted over the top of the spark plug, the signal in configuration VI is significantly lower as compared to the signal recorded with the photo diode that is mounted to the side of the spark plug. We attribute this to the ground strap of the spark plug which partially shields the generated plasma. The luminosity images integrated over 90 spark discharges shown in Fig.10 suggest that the spatial distribution of the plasma in configuration VI is smaller compared to configurations I, II and IV. This leads to the circumstance that effectively a larger relative portion of the plasma is shielded behind the ground strap. The conclusions drawn in the following sections use the photo diode signal that is not shielded by the ground strap (photo diode mounted

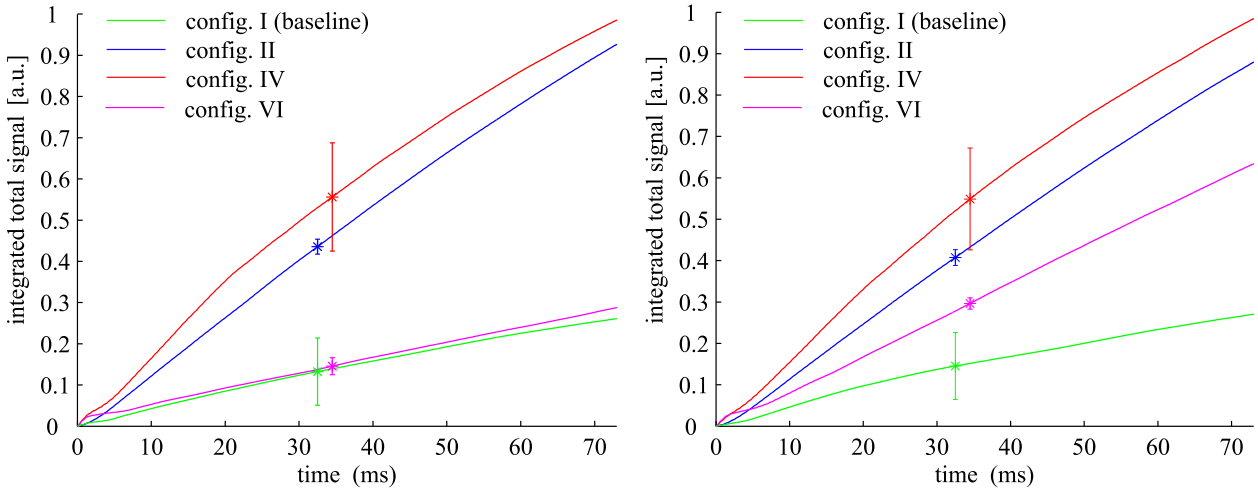

Figure 12. Time-integrated photo diode signals for the test configurations using the 0.54 mm spark gap. Photo diode mounted over the top of the spark plug is shown in the left hand side.

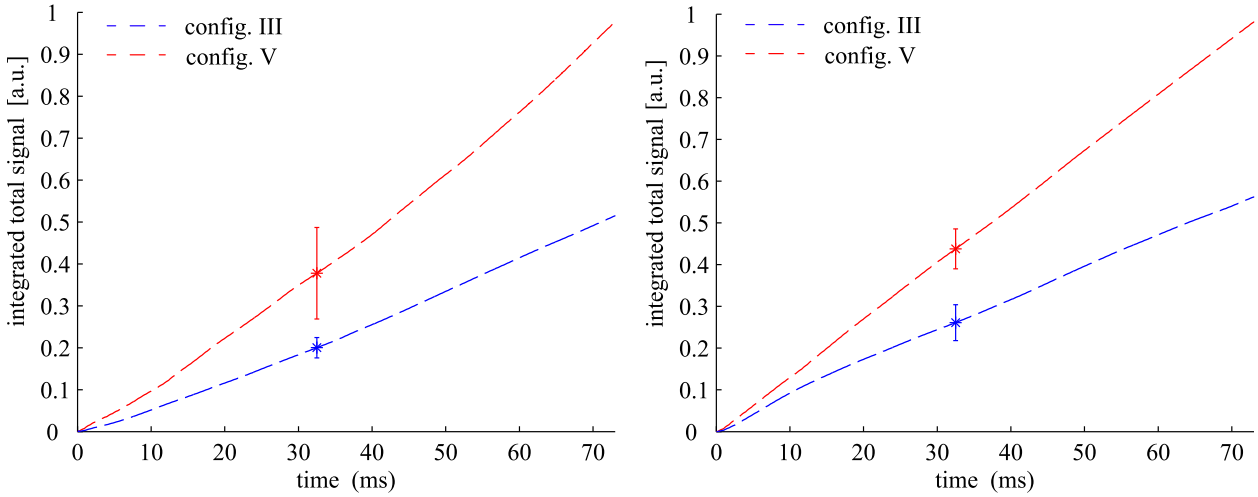

Figure 13. Time-integrated photo diode signals for the test configurations using the 0.74 mm spark gap. Photo diode mounted over the top of the spark plug is shown in the left hand side.

over the side of the spark plug, Fig. 12 right). The photo diode signals obtained for coil B and C for the 0.74-mm spark gap (configurations *III* and *V*) are shown in Fig. 13. The spark luminescence generated in configuration *V* is 180% of that generated in configuration *III*. The photo diode signals presented in Fig. 12 cannot compared to those of Fig. 13 due to the sensitivity of the alignment of the photo diodes which are perturbed when the spark plug is changed in the experimental setup.

V.E. Final Performance Comparisons

The experiments presented here have shown that significant increases in spark performance can be achieved by selecting larger, more efficient and more powerful ignition coils. A final comparison is shown in Fig. 14. For the 0.54-mm spark gap tests, temporally integrated luminescence recordings obtained from the high-speed camera, which also records the thermal radiation generated at the spark electrodes, show signals 400–500% of that of the baseline setup. The temporally integrated photo diode signals, which do not include the thermal radiation caused at the electrodes, show spark luminescence signals 350–450% of that of the baseline setup. Coil C outperforms coil B with photo diode signals reaching 112% for the 0.54 mm spark gap (Fig. 14, right) and 180% for the 0.75 mm spark gap (Fig. 13).

Increasing the spark plug gap by 37% leads to signals that are 230% for coil B and 140% for coil C compared to that of the baseline configuration for the first spark generated. Fig. 15 shows a comparison

between the two spark gaps. The increase in spark luminescence scales proportionally with the spark gap for coil C, with an approximately 40% increase in signal over the 75 ms of test time. This relationship is not observed with coil B, which for the large spark gap, shows spark signals lower than that of the small spark gap between 10–60 ms.

Adding capacitance to the secondary side of the ignition coil leads to significantly stronger sparks in the first few milliseconds of the test as indicated by the photo diode signals shown in Fig. 16. After several milliseconds, however, this setup causes significantly more heating at the spark electrodes while the spark luminescence signal evaluated through the photo diodes drops significantly, below the values achieved without using the capacitive ignition lead.

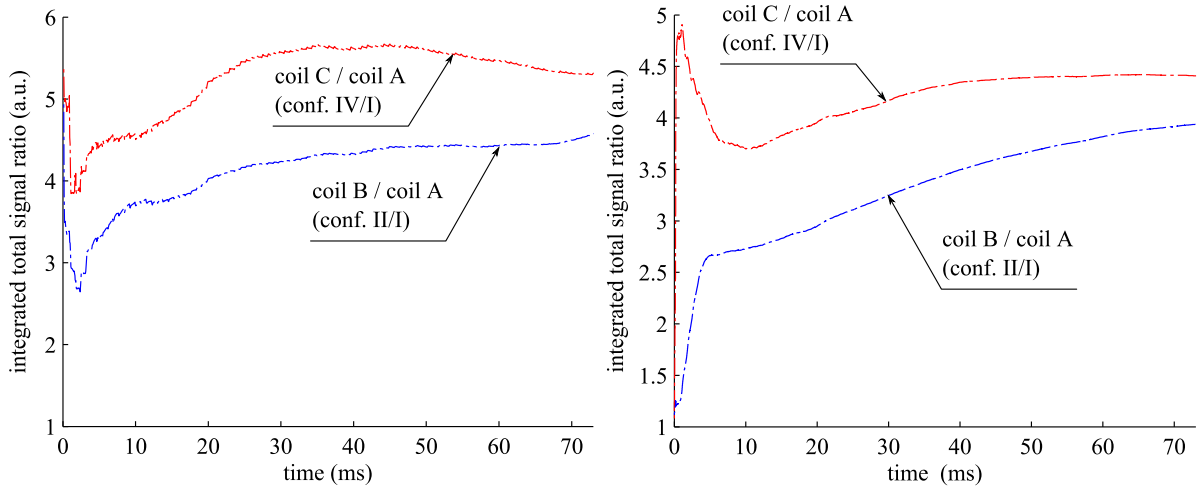

Figure 14. Relative performance of ignition coils B and C compared to ignition coil A. Evaluated using integrated luminescence recordings presented in Fig. 11 (left) as well as integrated (side) photodiode signals presented in Fig. 12 (right).

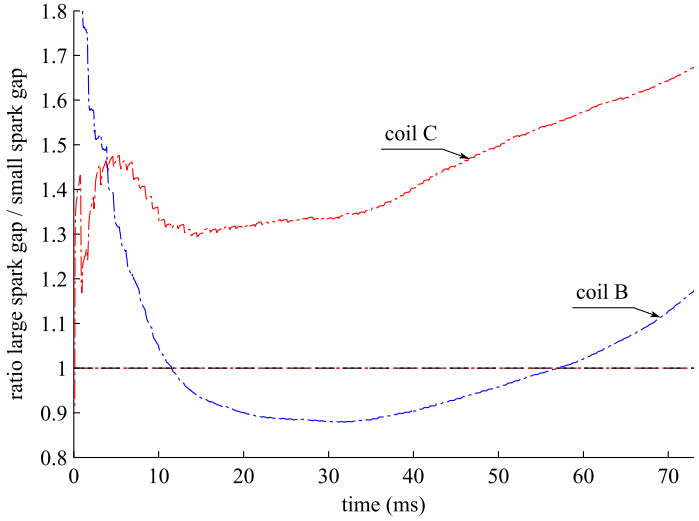

Figure 15. Increase in performance from increasing spark plug gap by 37% from 0.54 mm to 0.74 mm. Evaluated using integrated luminescence recordings presented in Fig. 11.

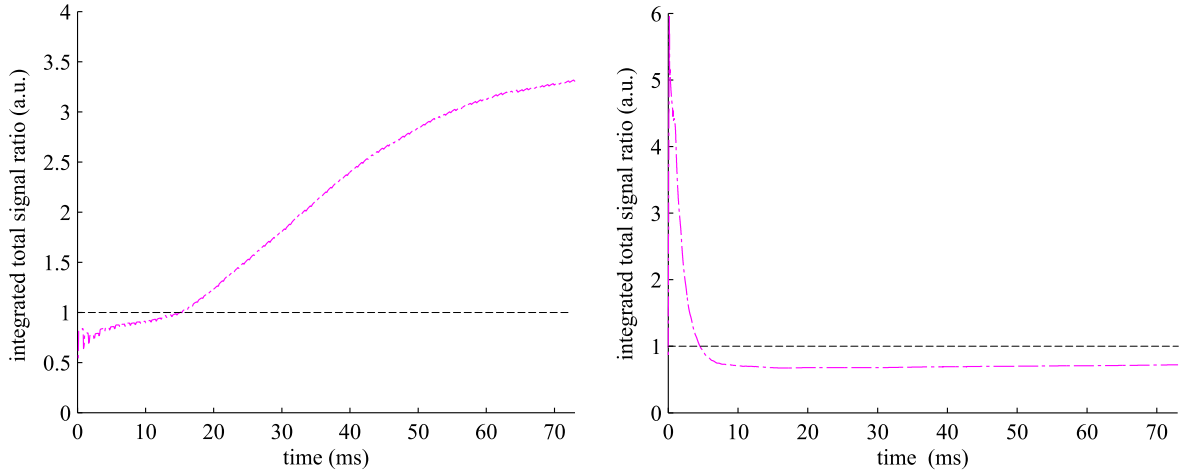

Figure 16. Relative performance comparison of standard and capacitive ignition lead (configuration VI and II). Evaluated using integrated luminescence recordings presented in Fig. 11 (left) as well as integrated (side) photodiode signals presented in Fig. 12 (right).

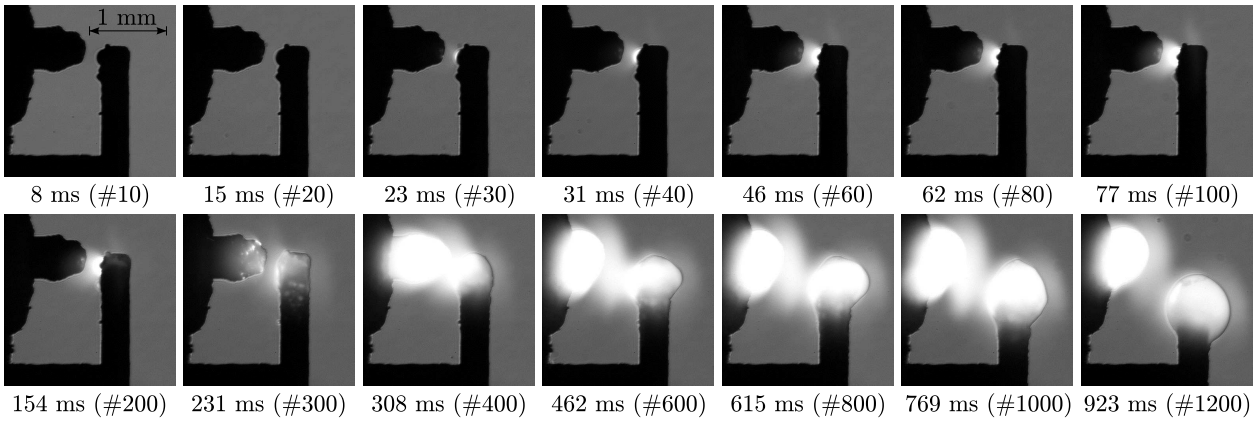

Figure 17. Luminescence recordings of molten electrodes providing a combined glow-spark plug capability taken after specified number of discharges.

V.F. Combined Glow-Spark Plug Setup

The comparison of the luminescence data obtained from the high-speed camera and the photo diode signals indicate that the electrodes of the spark plug heat up significantly during the 75 ms of test time. While the shape of the spark plug electrodes is not altered by the localized electrode heating during the 75-ms test time, the electrodes start to melt and are permanently deformed for test times longer than 250 ms as shown in Fig. 17. The transition from solid electrodes at high temperature to completely molten, liquid electrodes happens quickly within a few tens-of millisecond window. The images shown in Fig. 17 are images taken in between spark discharges, the high signals observed at the electrodes are purely thermal radiation from the heated and then molten electrodes. Spark discharges still occur between the molten electrodes, essentially providing a combined glow-spark plug function. Such a setup can be beneficial to cavity flameholding since it adds a continuous autoignition capability to the spark plug. A custom spark plug may be designed with heat transfer characteristics that allow the electrodes to heat up enough to provide a continuous autoignition capability to the spark plug without leading to complete melting of the electrodes.

V.G. Electrical energies on the secondary side of the ignition coil

This section presents a number of additional measurements where the spark energies on the secondary side of the ignition coil were assessed. The voltage on the secondary side was measured using a capacitive voltage divider and the current was measured using a current gun on the earth return line that is connected to the test cell/spark plug holder. The test cell is isolated from the ignition system ground and any current

ignition coil	*A*	*B*	*C*
manufacturer	Accel	Speedmaster	MSD Ignition
part number	140032	PCE 382.1009 (Pc 91)	HVC-2 8261
spark gap 1.47 mm, p = 0.5 atm			
E_{sec} [mJ]	14.4	30.8	46.3
spark gap 1.47 mm, p = 1.0 atm			
E_{sec} [mJ]	13.8	29.9	51.4
spark gap 0.74 mm, p = 1.0 atm			
E_{sec} [mJ]	13.4	23.1	42.0
E_{sec}/E_{pri}[%]	5.1	7.6	14.2
E_{sec}/E_{in}[%]	2.7	5.0	8.8

Table 6. Energies measured on the secondary side of the ignition coils and conversion efficiencies. The relative uncertainties for the energies measured on the secondary side of the ignition coils were evaluated as ≤5%.

flowing through the spark plug returns to the ignition box through this earth return. Table 6 shows the results of these measurements. The spark energies do not change significantly with varying spark gaps, the energy for the primary side of the ignition coil for coil A at a spark gap of 0.74 mm has not been measured, but was assumed to be identical to that for the 0.54 mm gap (Tab. 4). Using these measurements, we find a conversion efficiency for the ignition coil of 5.1% for coil A, 7.6% for coil B and 14.2% for coil C. The wall-plug efficiencies, that is the conversion efficiencies between the electrical input into the spark ignition unit and the electrical energy dissipated in the spark gap, have been evaluated as 2.7% for coil A, 5.0% for coil B and 8.8% for coil C, with no significant changes for different spark gaps. These wall plug efficiencies are evaluated from the electrical signals only and do not include the losses occurring when coupling this electric energy into the gas. The actual energies coupled into the gas have not been assessed, but the heating losses at the electrodes can be evaluated from the experiments presented in Fig. 17.

VI. Conclusions

We have characterized a capacitive-discharge spark ignition system that will be used for future cavity flameholding experiments in a Mach-7 scramjet engine. In the planned short-duration shock tunnel tests, that last only for a couple of milliseconds, the spark discharge is required to ignite a cavity flow that then acts as a flameholder for the neighboring supersonic flow. The ignition system operates with a maximum stable ignition frequency of 1300 Hz and requires approximately 0.6 kW of DC power at 18 V, which is equal to 0.04% of the theoretical combustor power. The average ignition coil input power is approximately 0.4 kW, and the spark energy at the ignition coil primary side is 300 mJ. The wall-plug efficiencies, that is the conversion efficiencies between the electrical input to the ignition system and the energy dissipated in the spark gap, have been evaluated as 2.7% for coil A, 5.0% for coil B and 8.8% for coil C, with no significant changes for different spark gaps. A number of different ignition system configurations have been tested to evaluate potential performance gains over the baseline configuration. The spark luminescence signal was used as a measure for the amount of plasma generated in the spark discharge. This luminescence signal was captured using a high-speed video camera and two photo diodes. The data shows that out of the three ignition coils tested, the low-resistance, closed-iron-core coil (coil C) generates the strongest spark discharge. The spatially and temporally integrated plasma luminescence signal recorded with the photo diode is 450% compared to that of the baseline configuration. Tests performed with a spark gap that was increased by 37% showed a proportional increase in discharge performance for this coil. Adding capacitance to the secondary side of the ignition coil has shown promising gains with luminescence signals reaching more than 500% compared to the respective baseline configuration for the first few discharges, however, the net-effect after that initial period is a reduced spark discharge luminescence and greatly increased electrode heating. The experiments have also shown, that the spark plug can be operated as a combined glow-spark plug, providing a continuous autoignition capability.

Acknowledgments

The authors gratefully acknowledge the technical and engineering support received by Keith Hitchcock, Barry Allsop and their colleagues at the Centre for Hypersonics, University of Queensland. This work was undertaken under AOARD Grant No. FA2386-13-1-4060.

References

[1]Smart, M. K., *Scramjets*, NATO-RTO-AVT, Rhode-Saint-Genèse, Belgium, 2008.

[2]Colket, M. B. and Spadaccini, L. J., "Scramjet fuels autoignition study," *Journal of Propulsion and Power*, Vol. 17, No. 2, 2001, pp. 315–323.

[3]Maurice, L. Q., Edwards, T., Cuoco, F., Bruno, C., and Hendrick, P., *Chapter 2: fuels*, in Technologies for Propelled Hypersonic Flight, NATO-RTO-AVT, National Technical Information Service, Virginia, USA, 2006.

[4]McBride, B. J. and Gordon, S., *Computer Program for Calculation of Complex Chemical Equilibrium Compositions and Applications*, Reference publication 1311, NASA Lewis Research Center, Cleveland, USA, 1996.

[5]Brieschenk, S., Kleine, H., and O'Byrne, S., "Laser ignition of hypersonic air-hydrogen flow," *Shock Waves*, Vol. 23, No. 5, 2013, pp. 439–452.

[6]Brieschenk, S., O'Byrne, S., and Kleine, H., "Laser-induced plasma ignition studies in a model scramjet engine," *Combustion and Flame*, Vol. 160, No. 1, 2013, pp. 145–148.

[7]Brieschenk, S., O'Byrne, S., and Kleine, H., "Ignition characteristics of laser-ionized fuel injected into a hypersonic crossflow," *Combustion and Flame*, Vol. 161, No. 4, 2013, pp. 1015–1025.

[8]Jacobsen, L. S., Carter, C. D., Baurle, R. A., and Jackson, T. A., *Toward plasma-assisted ignition in scramjets*, 3rd Workshop on thermochemical processes in plasma aerodynamics, Wright-Patterson Air Force Base, USA, 2003.

[9]Starikovskaia, S. M., "Plasma assisted ignition and combustion," *Journal of Physics D: Applied Physics*, Vol. 39, No. 16, 2006, pp. R265–R299.

[10]Starikovskiy, A. and Aleksandrov, N., "Plasma-assisted ignition and combustion," *Progress in Energy and Combustion Science*, Vol. 39, 2013, pp. 61–110.

[11]Do, H., Im, S. K., Cappelli, M. A., and Mungal, M. G., "Plasma assisted flame ignition of supersonic flows over a flat wall," *Combustion and Flame*, Vol. 157, No. 12, 2010, pp. 2298–2305.

[12]Takita, K., "Ignition and flame-holding by oxygen, nitrogen and argon plasma torches in supersonic airflow," *Combustion and Flame*, Vol. 128, No. 3, 2002, pp. 301–313.

[13]Kuo, S. P., Rubinraut, M., Popovic, S., and Bivolaru, D., "Characteristic Study of a Portable Arc Microwave Plasma Torch," *IEEE Transactions on Plasma Science*, Vol. 34, No. 6, 2006, pp. 2537–2544.

[14]Smart, M., "Design of Three-Dimensional Hypersonic Inlets with Rectangular-to-Elliptical Shape Transition," *Journal of Propulsion and Power*, Vol. 15, 1999, pp. 408–416.

[15]Smart, M. and Turner, J., "Application of Inlet Injection to a Three-Dimensional Scramjet at Mach 8," *AIAA Journal*, Vol. 48, 2010, pp. 829–838.

[16]Denman, Z. J., Brieschenk, S., Veeraravagan, A., Wheatley, V., and Smart, M. K., *Experimental Design of a Cavity Flameholder in a Mach 8 Shape-Transitioning Scramjet*, 19th AIAA International Space Planes and Hypersonic Systems and Technologies Conference, Atlanta, USA, 2014.

[17]Stalker, R. J. and Morgan, R. G., *The University of Queensland free piston shock tunnel T4 - initial operation and preliminary calibration*, 4th International Space Engineering Symposium, Brisbane, Australia., 1988.

[18]Stalker, R. J., Paull, A., Mee, D. J., Morgan, R. G., and Jacobs, P. A., "Scramjets and Shock Tunnels The Queensland Experience," *Progress in Aerospace Sciences*, Vol. 41, No. 6, 2005, pp. 471–453.

[19]Shapiro, A. H., *Dynamics and Thermodynamics of Compressible Fluid Flow, Vol. 1 and 2*, Ronald Press, New York, USA, 1953.

[20]O'Byrne, S., Doolan, M., Olsen, S. R., and Houwing, A. F. P., "Analysis of transient thermal choking processes in a model scramjet engine," *Journal of Propulsion and Power*, Vol. 16, No. 5, 2000, pp. 808–814.

[21]Murthy, S. N. B., *Basic performance assessment of scram combustors*, in Scramjet Propulsion, Curran, E. T. and Murthy, S. N. B. (eds), AIAA, Reston, USA, 2000.

[22]Pergament, H. S., *A theoretical analysis of non-equilibrium hydrogen-air reactions in flow systems*, AIAA/ASME Hypersonic Ramjet Conference, Naval Ordnance Laboratory, White Oak, USA, 1963.

[23]Chao, J. and Lee, J. H. S., "The propagation mechanism of high speed turbulent deflagrations," *Shock Waves*, Vol. 12, No. 4, 2002, pp. 277–289.

[24]Kim, H. J., Chung, S. H., and Sohn, C. H., "Numerical Calculation of Minimum Ignition Energy for Hydrogen and Methane Fuels," *KSME International Journal*, Vol. 18, No. 5, 2004, pp. 838–846.

[25]Calcote, H. F., Gregory, C. A., Barnett, C. M., and Gilmer, R. B., "Spark Ignition - Effect of Molecular Structure," *Industrial & Engineering Chemistry*, Vol. 44, No. 11, 1952, pp. 2656–2662.